

WEAKLY CONVEX RIDGE REGULARIZATION FOR 3D NON-CARTESIAN MRI RECONSTRUCTION

German Shâma Wache ¹, Chaithya G R ^{2,3}, Asma Tanabene^{2,3,4}, and Sebastian Neumayer ^{1,†}

¹Faculty of Mathematics, Chemnitz University of Technology, Germany

²NeuroSpin, Frédéric Joliot Institute for Life Sciences, CEA Paris-Saclay, France

³MIND, Inria Saclay Centre, France

⁴Siemens Healthineers, France

[†]Correspondence: sebastian.neumayer@math.tu-chemnitz.de

ABSTRACT

While highly accelerated non-Cartesian acquisition protocols significantly reduce scan time, they often entail long reconstruction delays. Deep learning-based reconstruction methods can alleviate this, but often lack stability and robustness to distribution shifts. As an alternative, we train a rotation-invariant weakly convex ridge regularizer (WCRR). The resulting variational reconstruction approach is benchmarked against state-of-the-art methods on retrospectively simulated data and (out-of-distribution) on prospective GoLF-SPARKLING and CAIPIRINHA acquisitions. Our approach consistently outperforms widely used baselines and achieves performance comparable to Plug-and-Play reconstruction with a state-of-the-art 3D DRUNet denoiser, while offering substantially improved computational efficiency and robustness to acquisition changes. In summary, WCRR unifies the strengths of principled variational methods and modern deep learning-based approaches.

Keywords inverse problems; medical imaging; parallel imaging; rotation invariance; variational reconstruction

1 INTRODUCTION

Magnetic resonance imaging (MRI) is a powerful technique enabling non-invasive visualization of anatomy and physiology with high soft-tissue contrast, which is key for the diagnosis of many medical conditions. The corresponding measurements are acquired sequentially, which is a time-consuming process with low throughput, high susceptibility to motion artifacts, and potential for patient discomfort. Parallel imaging techniques like SENSE [50] and GRAPPA [27] leverage spatial redundancy from multi-coil receiver arrays to accelerate acquisition by uniform Cartesian undersampling of the k -space measurements. Even higher acceleration can be achieved through variable density sampling (VDS) combined with compressed sensing (CS) techniques that exploit sparsity of the imaged object under an appropriate transform [42, 40, 15, 10]. Efficient VDS implementations require non-Cartesian sampling of k -space, such as spiral trajectories [43, 38], twisting radial lines [34] and rosette trajectories [46], which have been actually proposed long before the advent of CS to provide flexible k -space coverage.

Mathematically, the data acquisition is modeled with the Fourier transform [49, 21]. For each receiver coil $c \in \{1, \dots, C\}$ with sensitivity map \mathbf{S}_c (which is encoded into a diagonal matrix), the associated k -space measurement $\mathbf{y}_c \in \mathbb{C}^M$ obeys

$$\mathbf{y}_c = \mathcal{F}_\Omega \mathbf{S}_c \mathbf{x} + \mathbf{n}_c, \quad (1)$$

with $\mathbf{x} \in \mathbb{C}^N$ being the imaged object, \mathcal{F}_Ω being the Fourier transform at sample locations $\Omega = \{\mathbf{k}_m\}_{m=1}^M$ with

$$(\mathcal{F}_\Omega \mathbf{x})_m = \sum_{n=1}^N \mathbf{x}_n e^{-i2\pi \langle \mathbf{k}_m, \mathbf{r}_n \rangle}, \quad m = 1, \dots, M, \quad (2)$$

and $\mathbf{n} = [\mathbf{n}_1, \dots, \mathbf{n}_C]^T$ being additive white Gaussian noise that captures measurement errors. In practice, the sensitivities \mathbf{S}_c

are unknown and need to be estimated from the data \mathbf{y}_c through methods like ESPiRiT [61]. Stacking coils yields the linear forward model

$$\mathbf{y} = \mathbf{A} \mathbf{x} + \mathbf{n}, \quad (3)$$

with

$$\mathbf{y} = \begin{bmatrix} \mathbf{y}_1 \\ \vdots \\ \mathbf{y}_C \end{bmatrix} \quad \text{and} \quad \mathbf{A} = \begin{bmatrix} \mathcal{F}_\Omega \mathbf{S}_1 \\ \vdots \\ \mathcal{F}_\Omega \mathbf{S}_C \end{bmatrix}. \quad (4)$$

As we typically only have few samples $\mathbf{k}_1, \dots, \mathbf{k}_M$ according to a non-uniform density, recovering \mathbf{x} from (3) is an ill-posed inverse problem with high sensitivity to the noise \mathbf{n} . As a remedy, we pursue a variational reconstruction approach [58], where we minimize an objective consisting of a data-fidelity term and a regularization term \mathcal{R} (promoting desired properties of \mathbf{x}), namely

$$\hat{\mathbf{x}} = \arg \min_{\mathbf{x} \in \mathbb{C}^N} \frac{1}{2} \|\mathbf{A} \mathbf{x} - \mathbf{y}\|_2^2 + \lambda \mathcal{R}(\mathbf{x}), \quad (5)$$

where $\lambda > 0$ balances the terms. A typical CS-based regularizer for (5) is $\mathcal{R}(\mathbf{x}) = \|\Psi \mathbf{x}\|_1$, which promotes sparsity under a transform Ψ such as the gradient (leading to the total variation [57]) or Wavelets [19, 12].

On the other hand, deep-learning-based approaches have become the state-of-the-art for solving inverse problems, see for example the reviews [4, 47, 28]. However, several concerns regarding their trustworthiness for applications remain [24]. In contrast, the variational approach (5) is theoretically founded but cannot achieve the same reconstruction quality when paired with classical regularizers. Thus, several works aim at learning better ones, see [31] for an overview. One example is the (learnable) fields-of-experts regularizer [56], which was popularized as (weakly) convex ridge regularizer (WCRR) for

two-dimensional inverse problems in [25, 26]. Here, we extend and benchmark WCRR for a 3D non-cartesian parallel MRI setting. Our contributions are threefold:

1. **A principled, scalable prior for 3D MRI data:** We adapt the WCRR to complex-valued 3D inputs, while preserving its interpretability and optimization guarantees.
2. **Rotation invariance:** We incorporate rotation invariance to decrease the model size and improve data-efficiency as advocated in [3, 64].
3. **A comprehensive MRI evaluation:** We benchmark WCRR reconstruction against compressed sensing methods, Plug-and-Play, and unrolled network. This includes both retrospective simulated data and prospective real-world data.

2 RELATED WORK

If sufficiently many \mathbf{k}_m are given, we can use the adjoint with density compensation (DCp) to get the approximate inverse $\mathcal{F}_\Omega^{-1} \approx \mathcal{F}_\Omega^H \mathbf{D}$ with $\mathbf{D} = \text{diag}(\mathbf{w})$, where \mathbf{w} can be estimated iteratively as described in [48]. Generalizations of this approach are discussed in [35]. Due to its simplicity, DCp often serves as baseline and initialization for more sophisticated models. Below, we solely comment on learned reconstruction approaches.

Learned regularizers Prior work on learning regularizers \mathcal{R} for (5) is largely concentrated on 2D Cartesian MRI [36, 65, 68, 20]. A non-Cartesian setting was investigated in [37], and an extension to 3D Cartesian MRI was explored in [22]. For 3D non-Cartesian MRI, we are not aware of prior work that employs learned regularizers.

Unrolled models Unrolled networks such as Variational Networks [30], Learned Primal–Dual [1] or MoDL [2] are inspired by classical reconstruction methods such as (5). For non-Cartesian MRI, architectures such as Nonuniform Variational Networks [59] and NC-PDNet [52] incorporate DCp and proper approximations of \mathcal{F}_Ω to ensure stability. Unrolled methods require substantial training data and may be sensitive to distribution shifts (object, contrast, coils, trajectory, noise).

Plug-and-play Plug-and-play (PnP) approaches [62] replace the proximal operator appearing in iterative solvers for (5) by a denoiser. As special case, regularization by Denoising (RED) [54, 53] deploys the gradient of a regularizer. Both approaches perform well empirically; however, most convergence guarantees rely on assumptions such as nonexpansiveness or Jacobian symmetry [41], which are typically violated by state-of-the-art denoisers. More realistic conditions have been proposed for gradient-step denoisers [32, 33]. So far, these have been implemented only in 2D, where they are already computationally expensive and highly memory intensive, making their extension to 3D challenging.

3 METHOD

Throughout, we interpret complex-valued image volumes as 2-channel (real and imaginary) real-valued ones. First, we detail the architecture of the regularizer \mathcal{R} that we deploy within the reconstruction model (5). Then, we describe its efficient training based on a denoising task.

3.1 Rotation-invariant fields-of-experts

We restrict ourselves to the rotation-invariant fields-of-experts model

$$\mathcal{R}(\mathbf{x}) = |\mathcal{G}|^{-1} \sum_{\mathbf{R} \in \mathcal{G}} \sum_{j=1}^J \langle \mathbf{1}_{2N}, \psi_j(\mathbf{W}_j \mathbf{R} \mathbf{x}) \rangle, \quad (6)$$

where \mathcal{G} is a set of rotations, $\mathbf{W} = [\mathbf{W}_1, \dots, \mathbf{W}_J]^\top$ a stack of convolution operators acting on the rotated versions of $\mathbf{x} \in \mathbb{R}^{2N}$, and the potentials $\psi = [\psi_1, \dots, \psi_J]^\top$ with $\psi_j: \mathbb{R} \rightarrow \mathbb{R}$ are applied *component-wise*. The following proposition is the analog of [26, Prop. 3.2].

Proposition 1. *If the ψ_j are 1-weakly convex and $\|\mathbf{W}\| = 1$, then \mathcal{R} in (6) is also 1-weakly convex.*

Proof. A function $g: \mathbb{R}^m \rightarrow \mathbb{R}$ is ρ -weakly convex iff $g + \frac{\rho}{2} \|\cdot\|^2$ is convex. Hence, ζ_j with $z \mapsto \langle \mathbf{1}, \psi_j(\mathbf{z}) \rangle$ is 1-weakly convex because the ψ_j are 1-weakly convex. Moreover, we have for any linear map \mathbf{M} that

$$\begin{aligned} \zeta_j \circ \mathbf{M} + \frac{1}{2} \|\mathbf{M}\|^2 \|\cdot\|^2 \\ = (\zeta_j + \frac{1}{2} \|\cdot\|^2) \circ \mathbf{M} + \frac{1}{2} (\|\mathbf{M}\|^2 \|\cdot\|^2 - \|\mathbf{M} \cdot\|^2). \end{aligned} \quad (7)$$

Due to $\|\mathbf{M}\mathbf{x}\|^2 \leq \|\mathbf{M}\|^2 \|\mathbf{x}\|^2$, the second summand in (7) is convex. Thus, the composition $\zeta_j \circ \mathbf{M}$ is $\|\mathbf{M}\|^2$ -weakly convex. Now, we choose $\mathbf{M} = \mathbf{W}_j \mathbf{R}$ with $\|\mathbf{R}\| = 1$ and $\|\mathbf{W}_j\| \leq \|\mathbf{W}\| = 1$. Then each functional $\zeta_j(\mathbf{W}_j \mathbf{R} \cdot)$ is 1-weakly convex. As non-negative average of 1-weakly convex functions, \mathcal{R} is 1-weakly convex. \square

If the ψ_j are differentiable, we have that

$$\nabla \mathcal{R}(\mathbf{x}) = |\mathcal{G}|^{-1} \sum_{\mathbf{R} \in \mathcal{G}} \mathbf{R}^\top \mathbf{W}^\top \psi'_j(\mathbf{W} \mathbf{R} \mathbf{x}). \quad (8)$$

For any $\mathbf{x}, \mathbf{z} \in \mathbb{R}^{2N}$, we then get

$$\begin{aligned} \|\nabla \mathcal{R}(\mathbf{x}) - \nabla \mathcal{R}(\mathbf{z})\| \\ \leq |\mathcal{G}|^{-1} \sum_{\mathbf{R} \in \mathcal{G}} \|\mathbf{R}^\top\| \|\mathbf{W}^\top\| \|\psi'_j(\mathbf{W} \mathbf{R} \mathbf{x}) - \psi'_j(\mathbf{W} \mathbf{R} \mathbf{z})\|. \end{aligned} \quad (9)$$

Thus, if the ψ'_j are Lipschitz continuous, we get from (9) that the same holds for $\nabla \mathcal{R}$.

3.2 Parametrization

The architecture is illustrated in Figure 1. As trade-off between orientation diversity and computational efficiency, we adopt

$$\mathcal{G} = \{\text{Id}, \text{Rot}_{(x, \frac{\pi}{2})}, \text{Rot}_{(y, \frac{\pi}{2})}, \text{Rot}_{(z, \frac{\pi}{2})}\}, \quad (10)$$

i.e., the identity together with the three 90 degree rotations around the coordinate axes. Further, we learn (i) the potentials $\{\psi_j\}_{j=1}^J$, and (ii) the convolution operators $\{\mathbf{W}_j\}_{j=1}^J$. Below, we detail their parameterization.

Potentials As proposed in [31], we take the Huber function with shape parameter $\beta > 0$ given by

$$\phi_\beta^{\text{Huber}}(t) = \begin{cases} \frac{\beta}{2} t^2, & |t| \leq \beta^{-1}, \\ |t| - \frac{1}{2\beta}, & |t| > \beta^{-1}, \end{cases} \quad (11)$$

and define the 1-weakly convex potential

$$\phi_\beta = \phi_\beta^{\text{Huber}} - \phi_1^{\text{Huber}}. \quad (12)$$

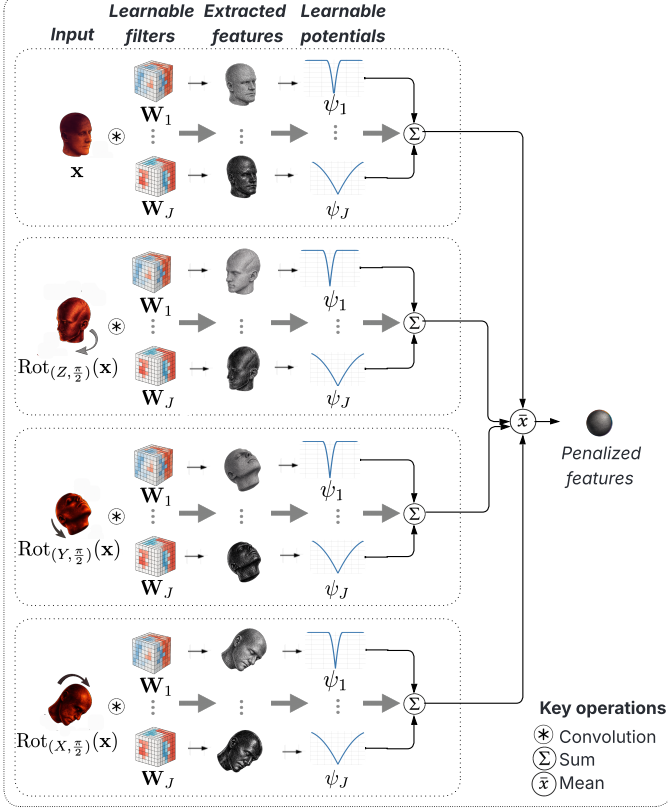


Figure 1: Illustration of WCRR: The (rotated) inputs are processed by a filter bank $\{\mathbf{W}_1, \dots, \mathbf{W}_J\}$. The extracted features are penalized based on the potentials $\{\psi_1, \dots, \psi_J\}$. Usually, the filters extract high-frequency information.

Following [26], we adapt ϕ_β per channel as

$$\psi_j = \frac{1}{\alpha_j^2} \phi_\beta(\alpha_j), \quad \alpha_j > 0, \quad (13)$$

with learnable parameters $\{\beta\} \cup \{\alpha_j\}_{j=1}^J$. Using a shared profile makes \mathcal{R} more interpretable and easier to analyze.

Convolutions To enforce $\|\mathbf{W}\|_2 = 1$, we proceed as in [26] and set

$$\mathbf{W} = \frac{\mathbf{U}}{\|\mathbf{U}\|}, \quad (14)$$

where \mathbf{U} denotes a 3D convolution operator. The spectral norm $\|\mathbf{U}\|$ is estimated using the discrete Fourier transform. Although this technically requires periodic boundary, we found it to be sufficiently accurate.

The operator \mathbf{U} is implemented as a cascade of three 3D convolutions with $3 \times 3 \times 3$ kernels, yielding an effective receptive field of $7 \times 7 \times 7$. The number of output channels are 8, 16, and 32, respectively. All convolutions are bias-free and use unit stride and grouping. Moreover, the kernels of the first layer have zero mean.

3.3 Training

As training task for the regularizer \mathcal{R}_θ in (6) with aggregated parameters θ , we consider denoising. To this end, let $\{\mathbf{x}^m\}_{m=1}^M$ denote a collection of clean training volumes. Each volume \mathbf{x}^m is

Algorithm 1 nmAPG

Require: Initialization \mathbf{x}_0 , initial Lipschitz estimate $L_1 > 0$, $\delta > 0$, $\eta \in (0, 1)$, $\rho \in (0, 1)$, line search steps K_L , tolerance $\epsilon > 0$.

```

1: Set  $\mathbf{z}_1 = \mathbf{x}_1 = \mathbf{x}_0$ ,  $t_1 = 1$ ,  $t_0 = 0$ ,  $q_1 = 1$ ,  $c_1 = \mathcal{J}(\mathbf{x}_1)$ 
2: while  $\|\mathbf{x}_k - \mathbf{x}_{k-1}\| / \|\mathbf{x}_{k-1}\| \geq \epsilon$  or  $k = 1$  do
3:    $\bar{\mathbf{x}}_k \leftarrow \mathbf{x}_k + \frac{t_{k-1}}{t_k}(\mathbf{z}_k - \mathbf{x}_k) + \frac{t_{k-1}-1}{t_k}(\mathbf{x}_k - \mathbf{x}_{k-1})$ 
4:   if  $k > 1$  then
5:      $L_k \leftarrow \frac{\langle \nabla \mathcal{J}(\bar{\mathbf{x}}_k) - \nabla \mathcal{J}(\bar{\mathbf{x}}_{k-1}), \nabla \mathcal{J}(\bar{\mathbf{x}}_k) - \nabla \mathcal{J}(\bar{\mathbf{x}}_{k-1}) \rangle}{\langle \nabla \mathcal{J}(\bar{\mathbf{x}}_k) - \nabla \mathcal{J}(\bar{\mathbf{x}}_{k-1}), \bar{\mathbf{x}}_k - \bar{\mathbf{x}}_{k-1} \rangle}$ 
6:   end if
7:    $c'_k \leftarrow \max\{\mathcal{J}(\bar{\mathbf{x}}_k), c_k\}$ 
8:   for  $l = 1, \dots, K_L$  do
9:      $\mathbf{z}_{k+1} \leftarrow \bar{\mathbf{x}}_k - \frac{1}{L_k} \nabla \mathcal{J}(\bar{\mathbf{x}}_k)$ 
10:    if  $\mathcal{J}(\mathbf{z}_{k+1}) \leq c'_k - \delta \|\mathbf{z}_{k+1} - \bar{\mathbf{x}}_k\|^2$  then
11:      break
12:    end if
13:     $L_k \leftarrow \frac{L_k}{\rho}$ 
14:  end for
15:  if  $\mathcal{J}(\mathbf{z}_{k+1}) \leq c_k - \delta \|\mathbf{z}_{k+1} - \bar{\mathbf{x}}_k\|^2$  then
16:     $\mathbf{x}_{k+1} \leftarrow \mathbf{z}_{k+1}$ 
17:  else
18:     $L_k \leftarrow \frac{\langle \nabla \mathcal{J}(\mathbf{x}_k) - \nabla \mathcal{J}(\bar{\mathbf{x}}_{k-1}), \nabla \mathcal{J}(\mathbf{x}_k) - \nabla \mathcal{J}(\bar{\mathbf{x}}_{k-1}) \rangle}{\langle \nabla \mathcal{J}(\mathbf{x}_k) - \nabla \mathcal{J}(\bar{\mathbf{x}}_{k-1}), \mathbf{x}_k - \bar{\mathbf{x}}_{k-1} \rangle}$ 
19:    for  $l = 1, \dots, K_L$  do
20:       $\mathbf{v}_{k+1} \leftarrow \mathbf{x}_k - \frac{1}{L_k} \nabla \mathcal{J}(\mathbf{x}_k)$ 
21:      if  $\mathcal{J}(\mathbf{v}_{k+1}) \leq c_k - \delta \|\mathbf{v}_{k+1} - \mathbf{x}_k\|^2$  then
22:        break
23:      end if
24:       $L_k \leftarrow L_k / \rho$ 
25:    end for
26:    if  $\mathcal{J}(\mathbf{z}_{k+1}) \leq \mathcal{J}(\mathbf{v}_{k+1})$  then
27:       $\mathbf{x}_{k+1} \leftarrow \mathbf{z}_{k+1}$ 
28:    else
29:       $\mathbf{x}_{k+1} \leftarrow \mathbf{v}_{k+1}$ 
30:    end if
31:  end if
32:   $t_{k+1} \leftarrow \frac{\sqrt{4t_k^2 + 1} + 1}{2}$ 
33:   $q_{k+1} \leftarrow \eta q_k + 1$ 
34:   $c_{k+1} \leftarrow \frac{\eta q_k c_k + \mathcal{J}(\mathbf{x}_{k+1})}{q_{k+1}}$ 
35:   $k \leftarrow k + 1$ 
36: end while
37: return minimizer  $\mathbf{x}_k$ 

```

corrupted as $\mathbf{y}^m = \mathbf{x}^m + \sigma^m \mathbf{n}^m$ with Gaussian noise $\mathbf{n}^m \sim \mathcal{N}(\mathbf{0}, \mathbf{I})$ and noise level $\sigma^m \in [\sigma_{\min}, \sigma_{\max}]$. Inserting the parametric regularizer \mathcal{R}_θ from (6) into (5) (without the operator \mathbf{A}) induces the denoiser

$$\mathcal{D}_\theta(\mathbf{y}) = \arg \min_{\mathbf{x} \in \mathbb{R}^{2N}} \frac{1}{2} \|\mathbf{x} - \mathbf{y}\|_2^2 + \mathcal{R}_\theta(\mathbf{x}). \quad (15)$$

Now, to deal with all $\sigma \in [\sigma_{\min}, \sigma_{\max}]$ simultaneously, we follow [26] and condition the α_j in (13) on σ via the modified parametrization

$$\alpha_j(\sigma) = \frac{\exp(s_{c_j}(\sigma))}{\sigma + 10^{-5}}, \quad \sigma \in [\sigma_{\min}, \sigma_{\max}], \quad (16)$$

where s_{c_j} is a learnable linear spline with K equidistant knots $\sigma_1 = \sigma_{\min}, \dots, \sigma_K = \sigma_{\max}$ and associated (learnable) values c_j .

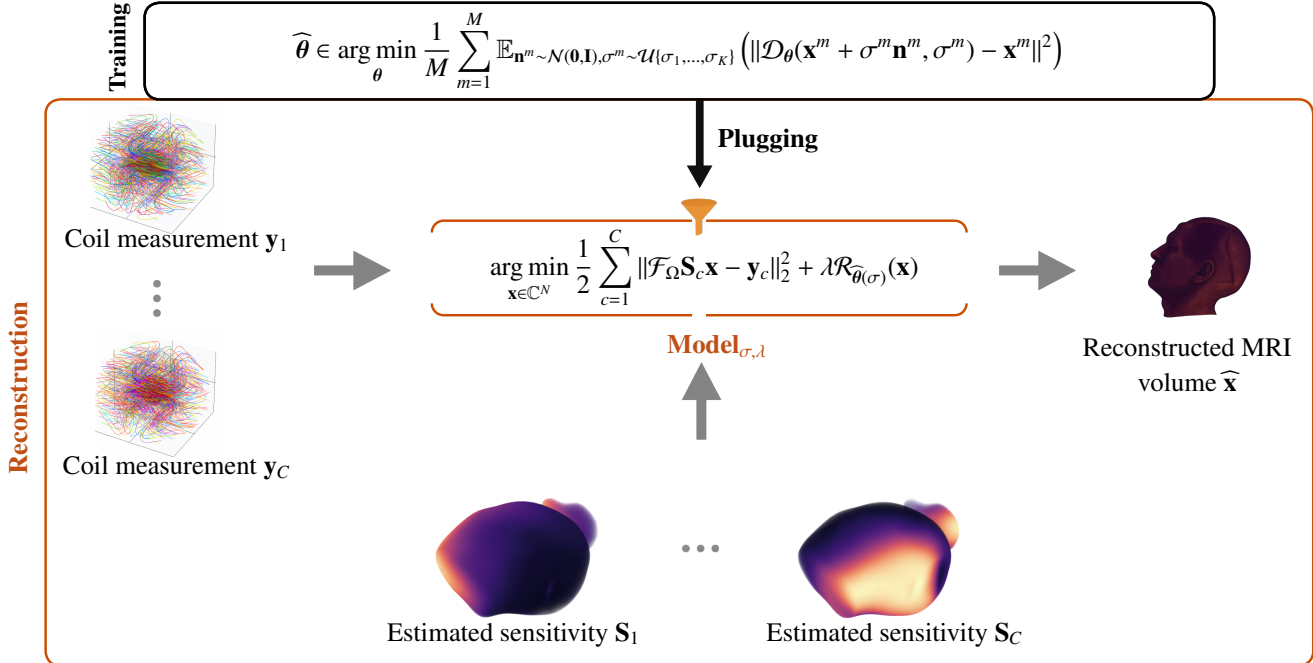


Figure 2: Overview of the training and reconstruction pipeline. The WCRR is trained on a Gaussian denoising task, and then used for MRI reconstruction. This involves only tuning of the scalar hyperparameters σ and λ of the reconstruction model on a (small) validation set. The coil sensitivity maps are estimated using the ESPIRiT algorithm [61] on the central 24×24 k-space data (simulating ACS acquisition).

This leads to the conditioned regularizer $\mathcal{R}_{\theta(\sigma)}$ with associated denoiser

$$\mathcal{D}_{\theta}(\mathbf{y}, \sigma) = \arg \min_{\mathbf{x} \in \mathbb{R}^{2N}} \frac{1}{2} \|\mathbf{x} - \mathbf{y}\|_2^2 + \mathcal{R}_{\theta(\sigma)}(\mathbf{x}). \quad (17)$$

To minimize the objective in (17), we choose the *non-monotone accelerated proximal gradient* (nmAPG) algorithm, which ensures global convergence to a minimum [39, Supp. Thm. 4]. The scheme is summarized for a generic objective \mathcal{J} in Algorithm 1. At each step k , a candidate \mathbf{z}_{k+1} for the next iterate \mathbf{x}_{k+1} is obtained through a gradient step taken from the extrapolation $\tilde{\mathbf{x}}_k$. If \mathbf{z}_{k+1} does not satisfy the non-monotone acceptance criterion, we compute a fallback candidate \mathbf{v}_{k+1} without the extrapolation and choose \mathbf{x}_{k+1} as the one with the lower energy \mathcal{J} . In both cases, the step size is initialized using a Barzilai–Borwein rule [6] and subsequently refined by a backtracking line search. In our experiments, we set $\delta = 0.1$, $\eta = 0.8$ and $\rho = 0.9$, and terminate the iterations when the relative change between consecutive iterates falls below $\epsilon = 1 \times 10^{-4}$.

For the multi-noise denoiser \mathcal{D}_{θ} , we seek the parameters θ that minimize the average reconstruction error over the dataset and all noise levels, namely

$$\hat{\theta} \in \arg \min_{\theta} \frac{1}{M} \sum_{m=1}^M \mathbb{E}_{(\mathbf{n}^m, \sigma^m)} \|\mathcal{D}_{\theta}(\mathbf{y}^m, \sigma^m) - \mathbf{x}^m\|_2^2. \quad (18)$$

We minimize the training loss (18) using the stochastic AdaBelief optimizer [67]. This involves the Jacobian $\mathbf{J}_{\theta} \mathcal{D}_{\theta}(\mathbf{y}, \sigma)$. To compute it, we adopt the implicit differentiation approach popularized for deep equilibrium models [5]. Specifically, we have that $\hat{\mathbf{x}}(\theta) = \mathcal{D}_{\theta}(\mathbf{y}, \sigma)$ satisfies the fixed-point condition

$$\hat{\mathbf{x}}(\theta) - \mathbf{y} + \nabla_{\mathbf{x}} \mathcal{R}_{\theta}(\hat{\mathbf{x}}(\theta)) = 0. \quad (19)$$

Applying the implicit-function theorem to (19) yields

$$(\mathbf{I} + \mathbf{H}_{\mathcal{R}}(\theta, \hat{\mathbf{x}}(\theta))) \mathbf{J}_{\theta} \hat{\mathbf{x}}(\theta) = \mathbf{J}_{\theta} (\nabla_{\mathbf{x}} \mathcal{R})(\theta, \hat{\mathbf{x}}(\theta)), \quad (20)$$

where $\mathbf{H}_{\mathcal{R}}$ denotes the Hessian of \mathcal{R}_{θ} with respect to \mathbf{x} . Matrix–vector products involving $\mathbf{J}_{\theta} \mathcal{D}_{\theta}$ are computed by solving the linear system (20) using the *minimum residual method*.

Training is performed with a batch size of 12 for 500 epochs using an initial learning rate of 1×10^{-2} and an exponential learning-rate schedule with a decay factor of $0.05^{1/500}$ per epoch. We use $M = 47$ training volumes (see Section 3.4) and randomly extract $64 \times 64 \times 64$ patches for each batch to improve computational efficiency. Regarding the noise range, we set $\sigma_{\min} = 0.01$, $\sigma_{\max} = 0.1$ and $K = 12$. Within each batch, every element is corrupted with a different noise level corresponding to one of the 12 spline knots. This maximizes the coverage of noise information, which we found to accelerate the training. This strategy can be extended to subsampling without replacement if the spline contains more knots than batch elements. Moreover, we regularize the training loss in (18) with

$$\mu \|\mathbf{H}_{\mathcal{R}}(\theta, \hat{\mathbf{x}}(\theta))\|_2, \quad (21)$$

namely the spectral norm of the Hessian of \mathcal{R} , with regularization strength $\mu = 1 \times 10^{-6}$ every five steps. The spectral norm is approximated using up to 50 power iterations. Empirically, this smoothness-promoting regularization resulted in parameter configurations for which nmAPG converged faster during evaluation.

3.4 MRI reconstruction

Given the regularizer (6), which is trained for denoising as described in Section 3.3, we now want to perform MRI reconstruction using variational reconstruction. As before, we minimize the reconstruction objective (5) with Algorithm 1. Since

the model was trained for denoising, we have to tune both the regularization parameter λ and the noise level σ of \mathcal{R} , for example with a grid search on a small validation set as described in Section 4. A summary of the complete training and reconstruction pipeline is given in Figure 2. Details on the data and the deployed sampling trajectory are provided below.

Training and validation data Our prospective simulations are conducted using the Cartesian raw k-space data from the *Calgary-Campinas* dataset [7], which provides 167 volumetric 3D T_1 -weighted gradient-echo brain scans acquired from healthy volunteers on a 3T scanner. The dataset includes 117 volumes collected with a 12-channel coil and 50 volumes acquired using a 32-channel coil. The train/validation/test split of the original dataset was 47/20/50 for 12-coil measurements and all the 50 32-coil measurements were used for test. All volumes admit partial Fourier sampling (up to 85%) along the slice-encoding direction (k_z). For numerical stability, we divide the measurements by 10^6 .

From these, we generated complex reference volumes by zero-filling the non-sampled regions, followed by an inverse fast Fourier transform. For the resulting per coil volumes, we applied virtual coil combination to obtain reference volumes. To ensure consistent dimensions, these are center-cropped to size $N_x \times N_y \times N_z = 256 \times 218 \times 170$. In the absence of a publicly available, high-quality 3D MRI database, we consider these volumes as a reasonable collection for training and benchmarking purposes without further post-processing.

Non-cartesian sampling trajectory In our experiments, we adopt the 3D GoLF-SPARKLING trajectory with GRAPPA acceleration [51], which relies on two complementary strategies: Cartesian undersampling of the k-space center and non-uniform sampling at higher frequencies. To this end, the trajectory readouts are designed to intersect the k-space center along straight Cartesian lines. Then, by modifying trajectory-specific affine constraints [13, 23], we ensure a structured, GRAPPA-like undersampling pattern for the center. In practice, we maintain a 2x2 pattern, concentrating approximately 60% of the measurements near the origin. In contrast, the remaining portion of the k-space follows a non-Cartesian sampling distribution to exploit the benefits of compressed sensing.

The trajectory consists of 4489 shots (readouts) with 416 samples each. A visualization is provided in Figure 3. The chosen design ensures robust low-frequency coverage and data consistency while preserving the efficiency of non-Cartesian SPARKLING sampling at high frequencies. It achieves an acceleration factor of $AF \approx 8.3$, resulting in a scan time of nearly 1 minute for a 1 mm isotropic whole brain MRI scan.

4 BENCHMARK SETUP

We compare WCRR to the reconstruction methods listed below. For their implementation, we rely on the *DeepInverse* library [60]. Moreover, we use the 3D non-uniform fast Fourier transform (NUFFT) implementation from *MRI-NUFFT* [16]. Our code is available on Github ¹.

GRAPPA + DCp GRAPPA performs a kernel-based interpolation to fill the missing values in the gridded region of the

¹<https://github.com/Shamachrist7/wcrr-noncartesian-3d-mri>

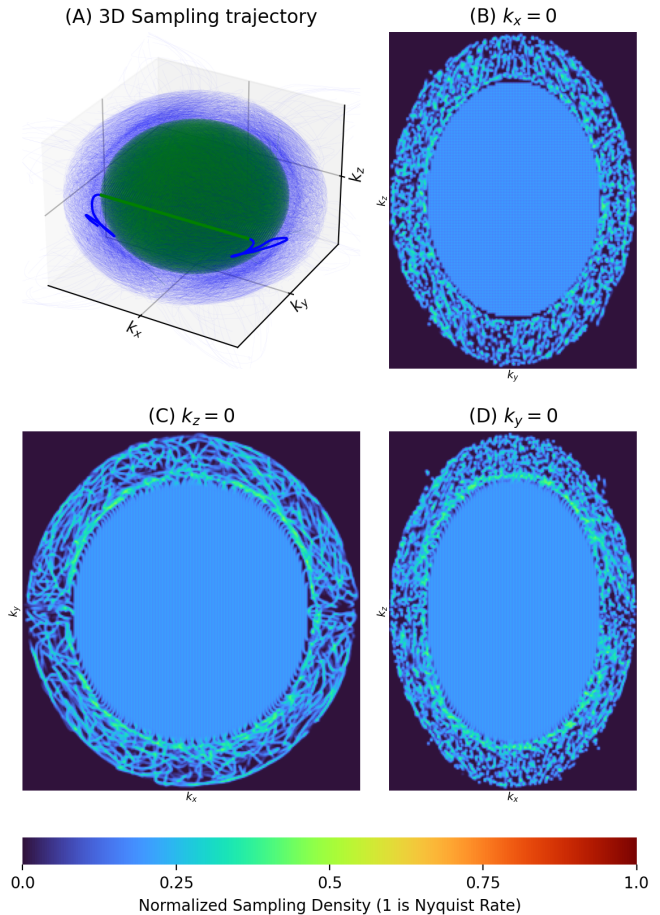


Figure 3: (A) 3D GoLF-SPARKLING trajectory with GRAPPA acceleration. The green portion highlights the central Cartesian readouts, and the blue one depicts the non-Cartesian SPARKLING parts. Slices with $\mathbf{k}_x = 0$, $\mathbf{k}_z = 0$, and $\mathbf{k}_y = 0$ are given in (B), (C) and (D), respectively.

k-space using neighboring values. We deploy a kernel with size $N_{k_x} \times N_{k_y} \times N_{k_z} = 5 \times 4 \times 4$. The GRAPPA kernel weights were fit based on the central 24×24 k-space lines, which correspond to the autocalibration signal (ACS) along with Tikhonov regularization with regularization parameter 10^{-4} . We then apply the DCp adjoint as approximate inverse.

ℓ_1 -wavelet This variational method is based on the regularizer $\mathcal{R}(\mathbf{x}) = \|[\Psi\mathbf{x}]_{\text{details}}\|_1$, where Ψ denotes the orthonormal 3D Daubechies-4 wavelet transform [18] with four decomposition levels (ignoring the approximation coefficients). The associated reconstruction problem (5) is solved using the *Fast Iterative Shrinkage-Thresholding Algorithm* (FISTA) [8]. The required proximal operator of \mathcal{R} has a closed-form (wavelet thresholding). In practice, we need to tune the regularization strength λ .

TV For reconstruction with isotropic TV regularization, we deploy a primal-dual scheme [17] with updates

$$\begin{aligned} \mathbf{p}_{k+1} &= \text{proj}_{\lambda\mathcal{B}_{2,\infty}}(\mathbf{p}_k + \eta\nabla\mathbf{x}_k) \\ \mathbf{x}_{k+1} &= \mathbf{x}_k - \tau(\mathbf{A}^T(\mathbf{A}\mathbf{x}_k - \mathbf{y}) + \nabla^\top(2\mathbf{p}_{k+1} - \mathbf{p}_k)), \end{aligned} \quad (22)$$

Iterative method	Regularization parameter λ	Denoising power σ
ℓ_1 -wavelet	0.003	–
TV	0.0001	–
WCRR	0.01	0.03
DPIR	5.5	0.002
NC-PDNet	–	–

Table 1: Retrospective simulation (Section 5.1): Adopted hyperparameters for each method.

where $\mathcal{B}_{2,\infty}$ denotes the unit ball for the grouped norm $\|\cdot\|_{2,\infty}$. To ensure convergence, we set $\tau = 1/\|A\|^2$, $\eta = 1/(24\tau)$ and $\mathbf{p}_0 = \mathbf{0} \in \mathbb{R}^{2N \times 3}$. Again, we need to tune the regularization strength λ .

NC-PDNet The NC-PDNet [52] is a 3D non-Cartesian extension of XPDNet, which ranked second in the fastMRI challenge [44]. It consists of 6 unrolled iterations of the Chambolle-Pock algorithm [14] with uncoupled parameters. As refinement backbone, we adopt a residual 3D U-Net [55], with three scales, SiLU activations, and 16–32–64 channels per scale, respectively. Each LPD step takes the previous two updates as input (extrapolation), and we trained the network using a combined L1–SSIM loss on magnitude differences. Note that our training set is comparatively small for an unrolled model.

Plug-and-play: DPIR DRUNet is a state-of-the-art learned denoiser [66]. A model trained for our data is available on Hugging Face². Following [66], we unroll the *Half Quadratic Splitting* algorithm for $K = 8$ iterations, leading to

$$\begin{aligned} \mathbf{u}_k &= \text{prox}_{\gamma_k \|A \cdot -y\|^2/2}(\mathbf{x}_k) \\ \mathbf{x}_{k+1} &= \mathcal{D}(\mathbf{u}_k, \sigma_k), \end{aligned} \quad (23)$$

with noise levels $\sigma_k = \sigma_{\text{init}}(\sigma/\sigma_{\text{init}})^{\frac{k}{k-1}}$ and stepsizes $\gamma_k = \lambda(\sigma_k/\sigma)^2$, where $\sigma_{\text{init}} = 0.01$. The tunable parameters are λ and σ .

Implementation Details and Tuning For all iterative methods, we initialize \mathbf{x}_0 with GRAPPA + DCp. We terminated all energy-based methods when the relative change between consecutive iterates drops below 5×10^{-3} , except for TV which required a smaller tolerance of 5×10^{-4} . After these thresholds, the reconstruction metrics remained constant. All hyperparameters were tuned with a grid search for the best reconstruction peak-signal-to-noise-ratio (PSNR) on a validation set consisting of 5 12-coil volumes from the validation split. The found parameters for the retrospective simulation in Section 5.1 are summarized in Table 1. The 32-coil setting remains as generalization task.

5 RESULTS

5.1 Retrospective simulation results

All reconstructions were performed on an *NVIDIA GeForce RTX 4070 Ti SUPER* with 16 GB memory. The overall peak GPU memory utilization recorded during reconstructions was found to be 7.01 GB.

²https://huggingface.co/deepinv/drune_3d_denoise_complex/tree/main

We generate non-Cartesian undersampled k-space data directly from the reconstructed and cropped per-coil MR images, see Section 3.4, and add white Gaussian noise with a standard deviation of $\sigma = 2 \times 10^{-3}$. From this data, we first compute the associated sensitivity maps \mathbf{S}_c using ESPiRiT [61]. The resulting data consistency operator $\mathcal{F}_\Omega \mathbf{S}_c$ is subsequently integrated into variational reconstruction and physics-informed deep learning models. For computational efficiency, we restrict ourselves to the first 10 measurements in both the 12- and 32-coil test datasets, selected in alphabetical order by name. The models are only fitted for the 12-coil setup and the 32-coil setup remains as a generalization task.

Quantitative results For quantitative evaluation, following the fastMRI protocol [44], PSNR and SSIM [63] (structural similarity index measure) were evaluated only within a foreground mask defined as the set of voxels whose magnitude exceeds 5% of the maximum ground-truth magnitude. This restricts the evaluation to anatomical regions and prevents bias caused by the large background area. The resulting metrics reported in Table 2 are averaged across all test volumes. Moreover, we provide the average runtime per reconstruction and the parameters for each method.

As expected, the parallel-imaging baseline (GRAPPA + DCp) provides the fastest reconstruction by a margin, but remains behind the other approaches in terms of reconstruction quality. The ℓ_1 -wavelet and TV methods improve reconstruction quality substantially at the cost of increased computation time. Despite being the only method trained specifically for the 12-coil configuration, the unrolled network NC-PDNet does not translate this training advantage into superior reconstruction quality. This is most likely due to the size of our training set, which is comparatively small for an unrolled network. Instead, the highest metrics for the 12-coil configuration are reached by DPIR and the proposed WCRR. However, DPIR struggles with the previously unseen 32-coil setup, suggesting limited generalization capability (potentially related to the patch-based application of the DRUNet). In contrast, WCRR performs very well in this unseen setting, outperforming all the other methods, while requiring four orders of magnitude fewer parameters than the deep learning alternatives. The distributions of the quantitative metrics across volumes reported in Figure 5 further reinforce the discussed findings. Finally, Figure 4 showcases a very important property of our WCRR: It is a convergent variational method. In particular, although we terminate the iterations with a relatively large tolerance of 5×10^{-3} , Algorithm 1 has essentially converged. Thus, its runtime remains comparable to classical iterative reconstruction baselines and much faster than the PnP approach DPIR.

Qualitative results Figure 6 reports qualitative comparisons on a 12-coil volume through sagittal, coronal, and transversal slices. Here, GRAPPA + DCp exhibits noticeable noise and residual aliasing, which partially obscures the thin white-matter boundaries. The ℓ_1 -wavelet and TV regularization reduce these artifacts but tend to oversmooth the fine structures, leading to slightly blurred edges.

For the coronal view, the zoom focuses on the region around the lateral ventricles and adjacent white-matter structures, whose sharp borders are important anatomical landmarks. Here, DPIR produces visually sharp boundaries, although some subtle textural inconsistencies appear in the

Method	12-coil			32-coil			# Params
	Masked PSNR	Masked SSIM	Runtime	Masked PSNR	Masked SSIM	Runtime	
GRAPPA + DCp	28.20	0.8035	7 s	35.62	0.9349	23 s	–
ℓ_1 -wavelet	29.80	0.8853	50 s	36.38	0.9561	1 min 51 s	–
TV	31.05	0.9158	1 min 51 s	<u>37.29</u>	<u>0.9665</u>	3 min 53 s	–
WCRR	31.58	<u>0.9320</u>	1 min 10 s	37.51	0.9708	1 min 57 s	8,377
DPIR	<u>31.40</u>	0.9321	6 min 38 s	35.35	0.9593	14 min 15 s	96,543,168
NC-PDNet	<u>30.10</u>	0.9201	<u>12 s</u>	32.52	0.9540	<u>31 s</u>	<u>6,670,584</u>

Table 2: Masked PSNR (dB), masked SSIM, and runtime of the different reconstruction methods for the 12-coil and 32-coil test data (unseen generalization task). The number of learnable parameters is given for learning-based approaches. In each column, the best value is highlighted in bold, and the second-best is underlined.

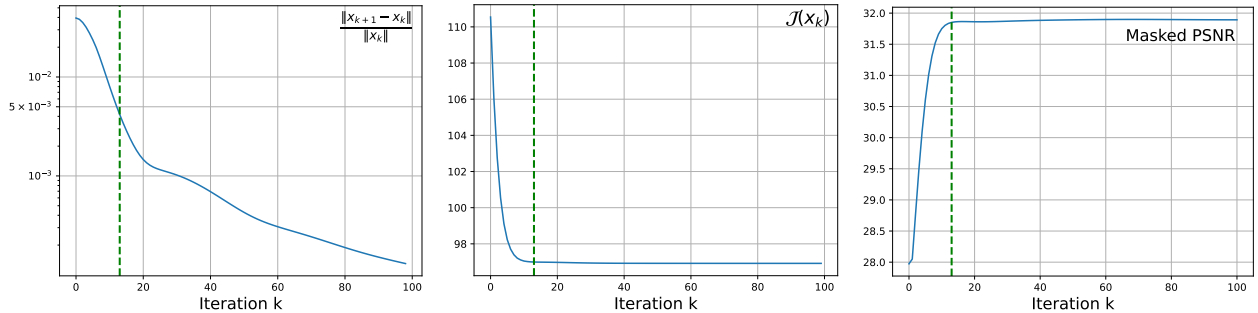


Figure 4: WCR convergence curves for reconstructing the 12-coil volume *e14091s3_P67584.7.h5*. (Left) Relative error between consecutive iterates (tolerance). (Middle) Energy functional. (Right) Masked PSNR. The dashed vertical line highlights where Algorithm 1 terminates with tolerance 5×10^{-3} .

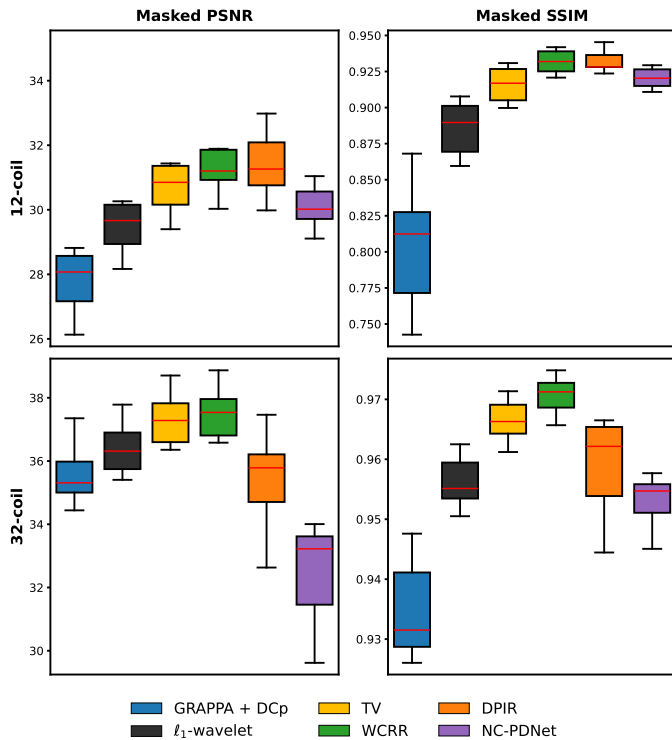


Figure 5: Box plots of the quantitative results (masked PSNR/masked SSIM) across volumes in the test sets.

periventricular white matter. Similar hallucination of structure was found for another 12-coil test volume and for even more of the 32-coil volumes. WCRR achieves a balanced reconstruction, preserving the ventricular contours and surrounding tissue contrast while maintaining a natural-looking texture. In the transversal (axial) slice, the highlighted region corresponds to complex gray- and white-matter interfaces. NC-PDNet produces relatively blurry structures in the zoomed region. Blurred traces of the exact same artefacts exhibited by the DPIR reconstruction can also be seen on the NC-PDNet reconstruction from a very close look. In contrast, WCRR preserves the anatomical interfaces of the basal ganglia region with clearer structural definition and fewer artifacts.

5.2 Out of distribution tests

We now showcase out-of-distribution results. For these, acquisitions were performed during the SENIOR cohort [29] scans at Neurospin with a 3T Siemens Healthineers Prisma^{fit} scanner and a 20-channel head coil. We utilized a clinically standard MPRAGE sequence with 1 mm isotropic resolution and whole-brain coverage. The parameters included TE/TR/TI of 3 ms/7.6 ms/800 ms, an MPRAGE-TR of 2.3 s, turbofactor of 176 and a flip angle of 9° . For ground truth reference, a fully sampled k-space acquisition was performed with a total scan time of nearly 9 minutes. For all the accelerated scans, external ACS acquisitions were obtained to estimate the sensitivity maps S_c through ESPiRIT [61]. All comparisons are purely qualitative due to potential inter-scan motion.

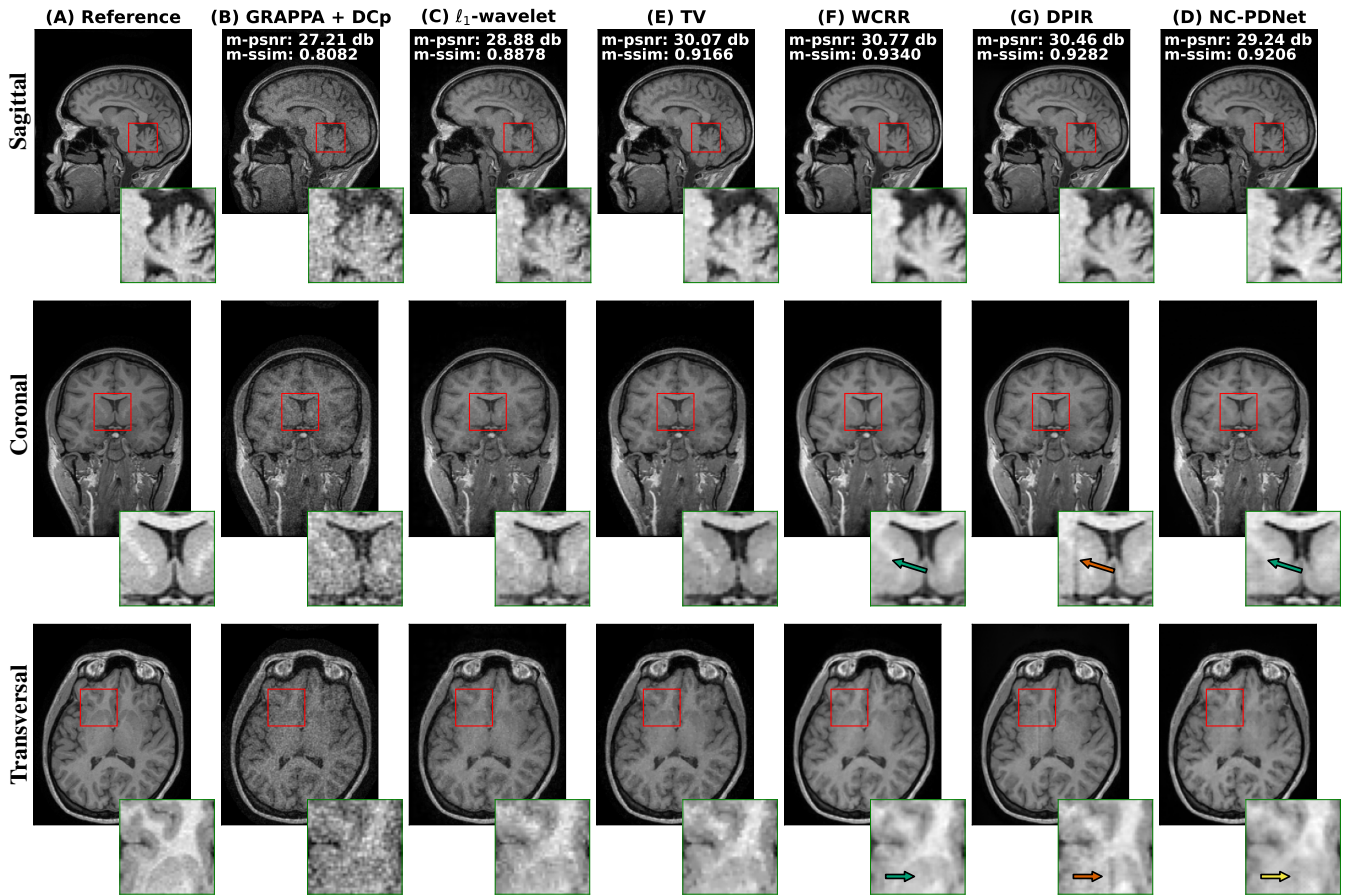


Figure 6: Cross-section (5th slice before the mid-slice) of the 12-coil volume *e14553s5_P44544.7.h5* along the *sagittal*, *coronal*, and *transversal* axes. The highlighted region is shown magnified in the corresponding inset. The shorthands m-psnr and m-ssim refer to the masked metrics. The green, yellow, and red arrows indicate good, okay, and bad behavior, respectively.

GS-SPARKLING with 2x2 GRAPPA We first tested all methods for acquisition based on the trajectory described in Section 3.4 with a total scan time of 1 minute. The results are given in Figure 7 along with zoomed in panes in sagittal, coronal and transversal views for easier qualitative comparison. For this data, the wavelet (C) and TV (D) reconstructions are a clear improvement over the SENSE reconstruction (B), but showcase blocky discontinuities and stair casing artifacts, respectively. As for our simulations, the best reconstruction results are achieved by WCRR (E) and DPIR (F) with significant reduction in image noise while preserving underlying structures. Finally, we notice that the reconstruction with NC-PDNet (G) is significantly blurry compared to other deep learning models. Apparently, the NC-PDNet would require re-training at a new and more suitable noise level.

CAIPIRINHA 3x2 We also evaluated the models in a highly accelerated Cartesian setting using a 1.5-minute accelerated acquisition with 3×2 CAIPIRINHA [11] (with $\Delta = 1$). Due to the absence of a corresponding sequence on the Siemens scanner, this acquisition was simulated by masking the fully sampled reference scan with a CAIPIRINHA undersampling pattern. The results are given in Figure 8. Noteworthy, unlike for non-Cartesian retrospective simulations, this approach closely matches a real prospective scan (as argued in [9]) since the

typical discrepancies of non-Cartesian data, such as NUFFT approximation errors, trajectory deviations, and off-resonance effects, are not present in this case. Here, the conventional SENSE reconstruction (B) exhibits significantly higher non-uniform spatial noise. While the wavelet reconstruction (C) still showcases blocky discontinuities, the best overall performance is achieved by TV (D) and WCRR (E), with only WCRR retaining the fine structural details in the transversal view. DPIR (F) fails to handle the non-uniform noise distribution, leaving visible residual noise in the sagittal view. Finally, as NC-PDNet (G) was never trained with the CAIPIRINHA undersampling pattern, it fails with significant blurring and loss of contrast. This showcases a typical problem of unrolled methods, namely that they require retraining if the evaluation protocol changes.

6 DISCUSSION AND CONCLUSION

We proposed WCRR for 3D MRI reconstruction, designed to balance reconstruction quality, computational efficiency, and algorithmic stability. Its close connection with compressed sensing approaches provides interpretability and increases trustworthiness compared to black box deep-learning approaches, which are both important considerations for clinical translation.

In our simulations, WCRR provides consistent and robust re-

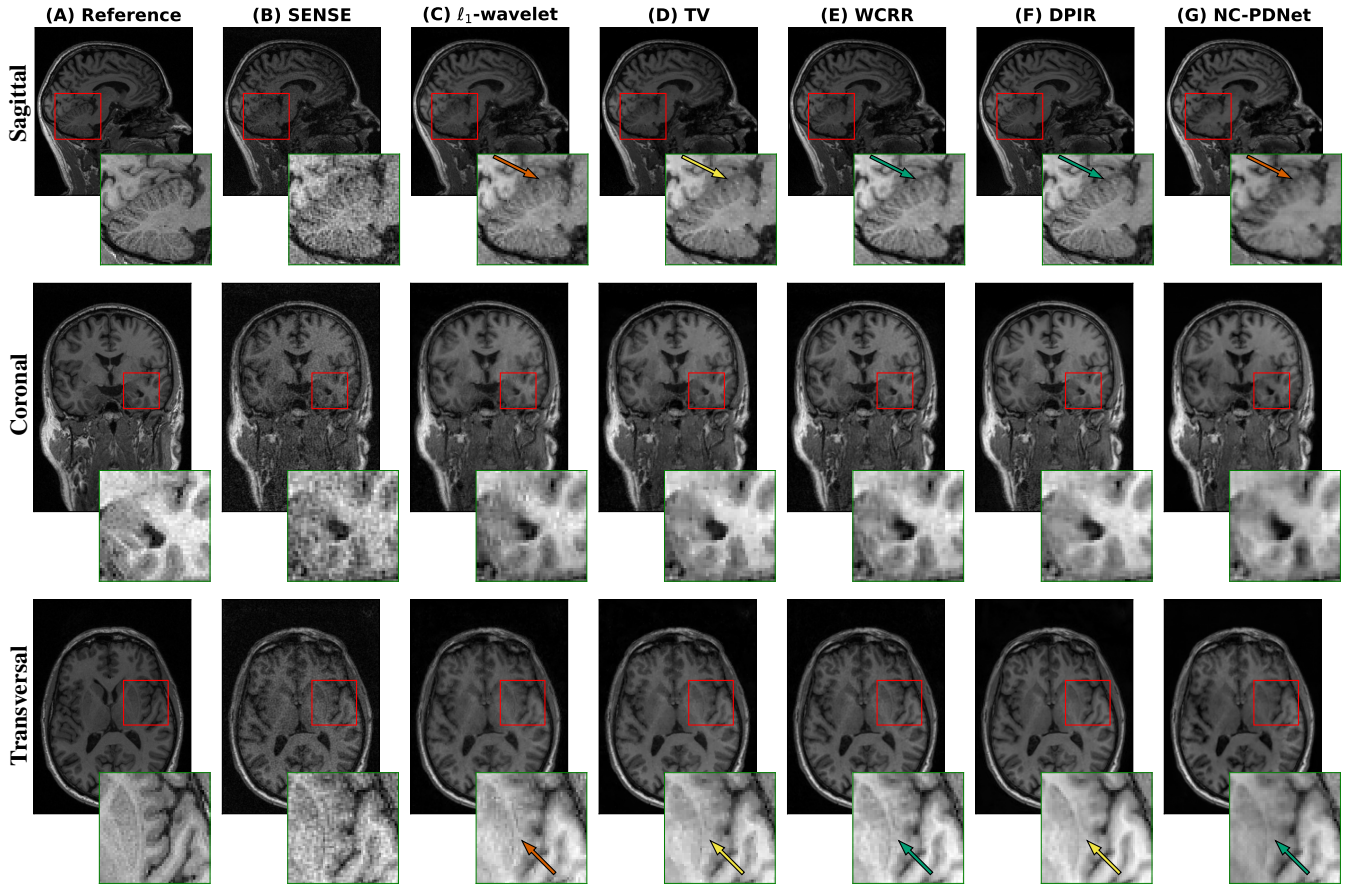


Figure 7: Mid plane reconstructions for GS-SPARKLING acquisitions with 2x2 GRAPPA (1 min) with (B) SENSE, (C) ℓ_1 -wavelets, (D) TV, (E) WCRR, (F) DPIR and (G) NC-PDNet. A reference volume (A) from a complete scan is also shown. We showcase *sagittal*, *coronal* and *transversal* views along with zoomed insets. The green, yellow, and red arrows indicate good, okay, and bad behavior, respectively.

constructions across varying coil configurations, which is particularly relevant in practice, where setups vary across scanners and sites. Quantitatively, WCRR achieves reconstruction quality at least on par with leading learning-based baselines. The qualitative evaluations demonstrate that WCRR preserves anatomical structures of clinical interest, including cortical boundaries and deep gray-matter regions, while effectively limiting noise amplification and residual aliasing. Most importantly, we did not find it to hallucinate structure. This is key in clinical workflows, where subtle structural differences may change the interpretation.

Below are two possible directions for future work. First, the rotation set \mathcal{G} was deliberately kept small to control computational cost, and more expressive orientation-aware designs could be explored. Second, replacing the constant vector $\mathbf{1}$ in (6) by spatially varying weights, as done in [45] for 2D inverse problems, could significantly improve the reconstruction quality.

Compliance with ethical Standards

This study was conducted retrospectively using human subject data made available in open access [7]. Ethical approval was not required as confirmed by the license attached with the open access data. All the prospective acquisitions were performed on

a healthy volunteer and with approvals from local and national ethical committees for the protocol, and after a written consent was obtained.

Acknowledgment

GSW and SN acknowledge support from the DFG within the SPP2298 under the Project Number 543939932. This work was granted access to the CCRT HPC facility under the Grant CCRT2026-tanaasma and CCRT2026-gilirach awarded by the Fundamental Research Division (DRF) of CEA. SN wants to thank Matthieu Terris for initiating this project through a discussion at BASP 2025.

Financial disclosure

None reported.

Conflict of interest

The authors declare no potential conflict of interests.

REFERENCES

- [1] J. Adler and O. Öktem. Learned primal-dual reconstruction. *IEEE Transactions on Medical Imaging*, 37(6):1322–1332, 2018.

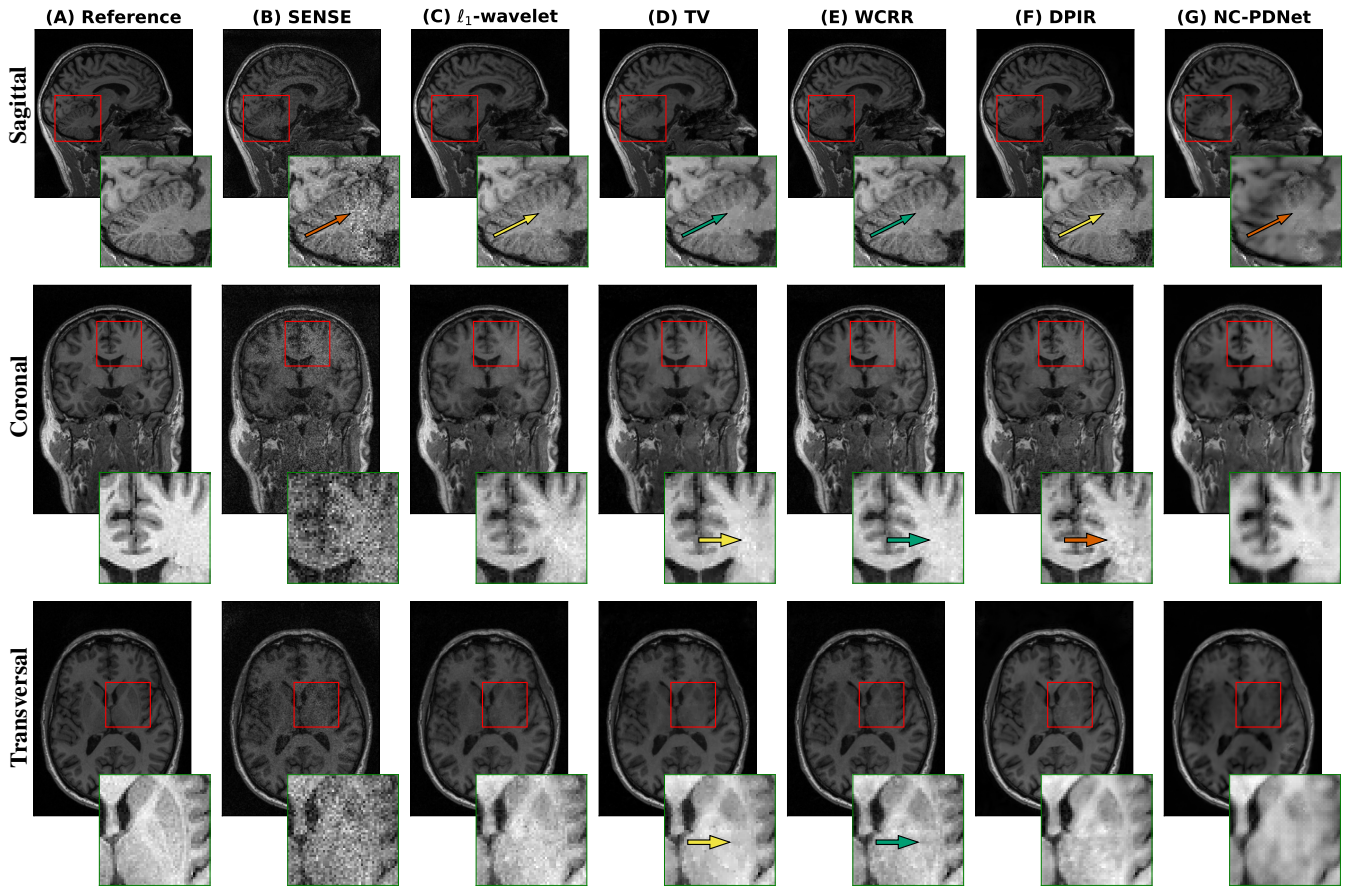


Figure 8: Mid plane reconstructions for simulated CAIPIRINHA 3x2 accelerated acquisitions (1.5 min) with (B) SENSE, (C) ℓ_1 -wavelets, (D) TV, (E) WCRR, (F) DPIR and (G) NC-PDNet. The corresponding ground truth reference (A) is also shown. We showcase *sagittal*, *coronal* and *transversal* views along with zoomed insets. The green, yellow, and red arrows indicate good, okay, and bad behavior, respectively.

- [2] H. K. Aggarwal, M. P. Mani, and M. Jacob. MoDL: Model-based deep learning architecture for inverse problems. *IEEE Transactions on Medical Imaging*, 38(2):394–405, 2018.
- [3] V. Andrearczyk, J. Fageot, V. Oreiller, X. Montet, and A. Depursinge. Exploring local rotation invariance in 3D CNNs with steerable filters. In *2nd International Conference on Medical Imaging with Deep Learning*, pages 15–26. PMLR, 2019.
- [4] S. Arridge, P. Maass, O. Öktem, and C.-B. Schönlieb. Solving inverse problems using data-driven models. *Acta Numerica*, 28:1–174, 2019.
- [5] S. Bai, J. Z. Kolter, and V. Koltun. Deep equilibrium models. In *Advances in Neural Information Processing Systems*, volume 32, pages 690–701. Curran Associates Inc., 2019.
- [6] J. Barzilai and J. M. Borwein. Two-point step size gradient methods. *IMA Journal of Numerical Analysis*, 8(1):141–148, 1988.
- [7] Y. Beauferris, J. Teuwen, D. Karkalousos, N. Moriakov, M. Caan, G. Yiasemis, L. Rodrigues, A. Lopes, H. Pedrini, L. Rittner, et al. Multi-coil MRI reconstruction challenge—assessing brain MRI reconstruction models and their generalizability to varying coil configurations. *Frontiers in Neuroscience*, 16:919186, 2022.
- [8] A. Beck and M. Teboulle. A fast iterative shrinkage-thresholding algorithm for linear inverse problems. *SIAM Journal on Imaging Sciences*, 2(1):183–202, 2009.
- [9] B. Bilgic, B. A. Gagoski, S. F. Cauley, A. P. Fan, J. R. Polimeni, P. E. Grant, L. L. Wald, and K. Setsompop. Wave-CAIPI for highly accelerated 3D imaging. *Magnetic Resonance in Medicine*, 73(6):2152–2162, 2014.
- [10] C. Boyer, J. Bigot, and P. Weiss. Compressed sensing with structured sparsity and structured acquisition. *Applied and Computational Harmonic Analysis*, 46(2):312–350, 2019.
- [11] F. A. Breuer et al. Controlled aliasing in parallel imaging results in higher acceleration (CAIPIRINHA) for multi-slice imaging. *Magnetic Resonance in Medicine*, 53(3):684–691, 2005.
- [12] E. J. Candès and M. B. Wakin. An introduction to compressive sampling. *IEEE Signal Processing Magazine*, 25(2):21–30, 2008.

- [13] G. R. Chaithya, P. Weiss, G. Daval-Fr erot, A. Massire, A. Vignaud, and P. Ciuciu. Optimizing full 3D SPARKLING trajectories for high-resolution magnetic resonance imaging. *IEEE Transactions on Medical Imaging*, 41(8):2105–2117, 2022.
- [14] A. Chambolle and T. Pock. A first-order primal-dual algorithm for convex problems with applications to imaging. *Journal of Mathematical Imaging and Vision*, 40(1):120–145, 2011.
- [15] N. Chauffert, P. Ciuciu, J. Kahn, and P. Weiss. Variable density sampling with continuous trajectories. *SIAM Journal on Imaging Sciences*, 7(4):1962–1992, 2014.
- [16] P.-A. Comby, G. Daval-Fr erot, C. Pan, A. Tanabene, L. Oudjman, M. Cencini, P. Ciuciu, and C. GR. MRI-NUFFT: Doing non-cartesian MRI has never been easier. *Journal of Open Source Software*, 10(108):7743, 2025.
- [17] L. Condat. A primal-dual splitting method for convex optimization involving Lipschitzian, proximable and linear composite terms. *Journal of Optimization Theory and Applications*, 158(2):460–479, 2013.
- [18] I. Daubechies. Orthonormal bases of compactly supported wavelets. *Communications on Pure and Applied Mathematics*, 41(7):909–996, 1988.
- [19] D. L. Donoho. De-noising by soft-thresholding. *IEEE Transactions on Information Theory*, 41(3):613–627, 1995.
- [20] M. A. G. Duff, N. D. F. Campbell, and M. J. Ehrhardt. Regularising inverse problems with generative machine learning models. *Journal of Mathematical Imaging and Vision*, 66:37–56, 2024.
- [21] J. A. Fessler and B. P. Sutton. Nonuniform fast Fourier transforms using min-max interpolation. *IEEE Transactions on Signal Processing*, 51(2):560–574, 2003.
- [22] N. Fuin, A. Bustin, T. K ustner, I. Oksuz, J. Clough, A. P. King, J. A. Schnabel, R. M. Botnar, and C. Prieto. A multi-scale variational neural network for accelerating motion-compensated whole-heart 3D coronary MR angiography. *Magnetic Resonance Imaging*, 70:155–167, 2020.
- [23] C. Giliyar Radhakrishna, G. Daval-Fr erot, A. Massire, A. Vignaud, and P. Ciuciu. Improving spreading projection algorithm for rapid k-space sampling trajectories through minimized off-resonance effects and gridding of low frequencies. *Magnetic Resonance in Medicine*, 90(3):1069–1085, 2023.
- [24] N. M. Gottschling, V. Antun, A. C. Hansen, and B. Adcock. The troublesome kernel: On hallucinations, no free lunches, and the accuracy-stability tradeoff in inverse problems. *SIAM Review*, 67(1):73–104, 2025.
- [25] A. Goujon, S. Neumayer, P. Bohra, S. Ducotterd, and M. Unser. A neural-network-based convex regularizer for inverse problems. *IEEE Transactions on Computational Imaging*, 9:781–795, 2023.
- [26] A. Goujon, S. Neumayer, and M. Unser. Learning weakly convex regularizers for convergent image-reconstruction algorithms. *SIAM Journal on Imaging Sciences*, 17(1):91–115, 2024.
- [27] M. A. Griswold, P. M. Jakob, R. M. Heidemann, M. Nitka, V. Jellus, J. Wang, B. Kiefer, and A. Haase. Generalized autocalibrating partially parallel acquisitions (GRAPPA). *Magnetic Resonance in Medicine*, 47(6):1202–1210, 2002.
- [28] A. Habring and M. Holler. Neural-network-based regularization methods for inverse problems in imaging. *GAMM-Mitteilungen*, 47(4):e202470004, 2024.
- [29] A. Haeger et al. Imaging the aging brain: study design and baseline findings of the senior cohort. *Alzheimer’s Research and Therapy*, 12(1), 2020.
- [30] K. Hammernik, T. Klatzer, E. Kobler, M. P. Recht, D. K. Sodickson, T. Pock, and F. Knoll. Learning a variational network for reconstruction of accelerated MRI data. *Magnetic Resonance in Medicine*, 79(6):3055–3071, 2018.
- [31] J. Hertrich, H. S. Wong, A. Denker, S. Ducotterd, Z. Fang, M. Haltmeier,  eljko Kereta, E. Kobler, O. Leong, M. S. Salehi, C.-B. Sch onlieb, J. Schwab, Z. Shumaylov, J. Sulam, G. S. Wache, M. Zach, Y. Zhang, M. J. Ehrhardt, and S. Neumayer. Learning regularization functionals for inverse problems: A comparative study. *arXiv preprint arXiv:2510.01755*, 2025.
- [32] S. Hurault, A. Leclaire, and N. Papadakis. Gradient step denoiser for convergent plug-and-play. In *10th International Conference on Learning Representations*, 2022.
- [33] S. Hurault, A. Leclaire, and N. Papadakis. Proximal denoiser for convergent plug-and-play optimization with nonconvex regularization. In *39th International Conference on Machine Learning*, pages 9483–9505. PMLR, 2022.
- [34] J. I. Jackson, D. G. Nishimura, and A. Macovski. Twisting radial lines with application to robust magnetic resonance imaging of irregular flow. *Magnetic Resonance in Medicine*, 25(1):128–139, 1992.
- [35] M. Kircheis and D. Potts. Fast and direct inversion methods for the multivariate nonequispaced fast Fourier transform. *Frontiers in Applied Mathematics and Statistics*, 9:1155484, 2023.
- [36] E. Kobler, A. Effland, K. Kunisch, and T. Pock. Total deep variation for linear inverse problems. In *Proceedings of the IEEE/CVF Conference on Computer Vision and Pattern Recognition*. IEEE, 2020.
- [37] A. Kofler, M. Haltmeier, T. Schaeffter, M. Kachelrie , M. Dewey, C. Wald, and C. Kolbitsch. Neural networks-based regularization for large-scale medical image reconstruction. *Physics in Medicine & Biology*, 65(13):135003, 2020.

- [38] C. S. Law and G. H. Glover. Interleaved spiral-in/out with application to functional MRI (fMRI). *Magnetic Resonance in Medicine*, 62(3):829–834, 2009.
- [39] H. Li and Z. Lin. Accelerated proximal gradient methods for nonconvex programming. In *Advances in Neural Information Processing Systems*, volume 28, pages 379–387. Curran Associates Inc., 2015.
- [40] B. Liu, Y. M. Zou, and L. Ying. SparseSENSE: Application of compressed sensing in parallel MRI. In *2008 International Conference on Technology and Applications in Biomedicine*, pages 127–130. IEEE, 2008.
- [41] J. Liu, S. Asif, B. Wohlberg, and U. Kamilov. Recovery analysis for plug-and-play priors using the restricted eigenvalue condition. In *Advances in Neural Information Processing Systems*, volume 34, pages 5921–5933. Curran Associates Inc., 2021.
- [42] M. Lustig, D. Donoho, and J. M. Pauly. Sparse MRI: The application of compressed sensing for rapid MR imaging. *Magnetic Resonance in Medicine*, 58(6):1182–1195, 2007.
- [43] C. H. Meyer, B. S. Hu, D. G. Nishimura, and A. Macovski. Fast spiral coronary artery imaging. *Magnetic Resonance in Medicine*, 28(2):202–213, 1992.
- [44] M. J. Muckley, B. Riemenschneider, A. Radmanesh, S. Kim, G. Jeong, J. Ko, Y. Jun, H. Shin, D. Hwang, M. Mostapha, S. Arberet, D. Nickel, Z. Ramzi, P. Ciuciu, J.-L. Starck, J. Teuwen, D. Karkalousos, C. Zhang, A. Sri-ram, Z. Huang, N. Yakubova, Y. W. Lui, and F. Knoll. Results of the 2020 fastMRI challenge for machine learning MR image reconstruction. *IEEE Transactions on Medical Imaging*, 40(9):2306–2317, 2021.
- [45] S. Neumayer and F. Altekruiger. Stability of data-dependent ridge-regularization for inverse problems. *Inverse Problems*, 41(6):065006, 2025.
- [46] D. C. Noll. Multishot rosette trajectories for spectrally selective MR imaging. *IEEE Transactions on Medical Imaging*, 16(4):372–377, 1997.
- [47] G. Ongie, A. Jalal, C. A. Metzler, R. G. Baraniuk, A. G. Dimakis, and R. Willett. Deep learning techniques for inverse problems in imaging. *IEEE Transactions on Information Theory*, 1(1):39–56, 2020.
- [48] J. G. Pipe and P. Menon. Sampling density compensation in MRI: Rationale and an iterative numerical solution. *Magnetic Resonance in Medicine*, 41(1):179–186, 1999.
- [49] D. Potts, G. Steidl, and M. Tasche. Fast Fourier transforms for nonequispaced data: A tutorial. In *Modern Sampling Theory: Mathematics and Applications*, pages 247–270. Birkhäuser, 2001.
- [50] K. P. Pruessmann, M. Weiger, M. B. Scheidegger, and P. Boesiger. SENSE: Sensitivity encoding for fast MRI. *Magnetic Resonance in Medicine*, 42(5):952–962, 1999.
- [51] C. G. Radhakrishna, A. Vignaud, M. Bertrait, A. Massire, M. Bottlaender, and P. Ciuciu. Bringing GRAPPA to non-Cartesian MRI through SPARKLING: An application to MPRAGE anatomical MRI. In *ISMRM & ISMRT Annual Meeting*, 2025.
- [52] Z. Ramzi, C. GR, J.-L. Starck, and P. Ciuciu. NC-PDNet: A density-compensated unrolled network for 2D and 3D non-Cartesian MRI reconstruction. *IEEE Transactions on Medical Imaging*, 41(7):1625–1638, 2022.
- [53] E. T. Reehorst and P. Schniter. Regularization by denoising: Clarifications and new interpretations. *IEEE Transactions on Computational Imaging*, 5(1):52–67, 2018.
- [54] Y. Romano, M. Elad, and P. Milanfar. The little engine that could: Regularization by denoising (RED). *SIAM Journal on Imaging Sciences*, 10(4):1804–1844, 2017.
- [55] O. Ronneberger, P. Fischer, and T. Brox. U-Net: Convolutional networks for biomedical image segmentation. In *Medical Image Computing and Computer-Assisted Intervention – MICCAI 2015*, page 234–241. Springer International Publishing, 2015.
- [56] S. Roth and M. J. Black. Fields of experts. *International Journal of Computer Vision*, 82(2):205–229, 2009.
- [57] L. I. Rudin, S. Osher, and E. Fatemi. Nonlinear total variation based noise removal algorithms. *Physica D: Nonlinear Phenomena*, 60(1–4):259–268, 1992.
- [58] O. Scherzer, M. Grasmair, H. Grossauer, M. Haltmeier, and F. Lenzen. *Variational Methods in Imaging*. Springer, 2009.
- [59] J. Schlemper, S. S. M. Salehi, P. Kundu, C. Lazarus, H. Dyvorne, D. Rueckert, and M. Sofka. Nonuniform variational network: deep learning for accelerated nonuniform mr image reconstruction. *International Conference on Medical Image Computing and Computer-Assisted Intervention*, pages 57–64, 2019.
- [60] J. Tachella, M. Terris, S. Hurault, A. Wang, D. Chen, M.-H. Nguyen, M. Song, T. Davies, L. Davy, J. Dong, et al. Deepinverse: A python package for solving imaging inverse problems with deep learning. *Journal of Open Source Software*, 10(115):8923, 2025.
- [61] M. Uecker, P. Lai, M. J. Murphy, P. Virtue, M. Elad, J. M. Pauly, S. S. Vasanawala, and M. Lustig. ES-PIRiT—an eigenvalue approach to autocalibrating parallel MRI: where SENSE meets GRAPPA. *Magnetic Resonance in Medicine*, 71(3):990–1001, 2014.
- [62] S. V. Venkatakrisnan, C. A. Bouman, and B. Wohlberg. Plug-and-play priors for model based reconstruction. In *IEEE Global Conference on Signal and Information Processing*, pages 945–948. IEEE, 2013.
- [63] Z. Wang, A. C. Bovik, H. R. Sheikh, and E. P. Simoncelli. Image quality assessment: From error visibility to structural similarity. *IEEE Transactions on Image Processing*, 13(4):600–612, 2004.

- [64] M. Winkels and T. S. Cohen. Pulmonary nodule detection in CT scans with equivariant CNNs. *Medical Image Analysis*, 55:15–26, 2019.
- [65] M. Zach, F. Knoll, and T. Pock. Stable deep MRI reconstruction using generative priors. *IEEE Transactions on Medical Imaging*, 42(12):3817–3832, 2023.
- [66] K. Zhang, Y. Li, W. Zuo, L. Zhang, L. Van Gool, and R. Timofte. Plug-and-play image restoration with deep denoiser prior. *IEEE Transactions on Pattern Analysis and Machine Intelligence*, 44(10):6360–6376, 2022.
- [67] J. Zhuang, T. Tang, Y. Ding, S. C. Tatikonda, N. Dvornik, X. Papademetris, and J. Duncan. Adabelief optimizer: Adapting stepsizes by the belief in observed gradients. In *Advances in Neural Information Processing Systems*, volume 33, pages 18795–18806. Curran Associates Inc., 2020.
- [68] Z. Zou, J. Liu, B. Wohlberg, and U. S. Kamilov. Deep equilibrium learning of explicit regularization functionals for imaging inverse problems. *IEEE Open Journal of Signal Processing*, 4:390–398, 2023.